JOURNAL OF GEOPHYSICAL RESEARCH, VOL. 114, A11210, doi:10.1029/2009JA014343, 2009

Click Here for Full Article

Asymmetric magnetic reconnection in the presence of a guide field

P. L. Pritchett[1] and F. S. Mozer[2]

Received 8 April 2009; revised 30 June 2009; accepted 7 August 2009; published 25 November 2009.

[1] The properties of asymmetric magnetic reconnection in the presence of a guide magnetic field are investigated using two-dimensional particle-in-cell simulations. The reconnection process is initiated by applying a spatially localized and temporally steady convection electric field at the high-density/low-magnetic-field (magnetosheath) side of the current layer. The in-plane Hall currents are dominated by the electron flows along the separatrices from the high-density to low-density side of the layer, and they strongly enhance the out-of-plane magnetic field in one hemisphere and decrease it in the other. On the enhanced magnetic field side are situated a bipolar pair of parallel electric fields and an electron velocity shear flow layer, both of which extend several ion inertia lengths (d_i) away from the X line. The shear flow layer is unstable to the generation of small-scale ($\ll d_i$) electron vortices which propagate away from the X line and produce a reduction of the order of 30% in the magnitude of the B_y field. An example of such a large-amplitude, short-duration depression in B_y is identified in a magnetopause crossing by the THEMIS spacecraft. The Ohm's law $(\mathbf{E} + \mathbf{U}_e \times \mathbf{B}/c)_y = 0$ is violated in this parallel field/velocity shear region, and the deviation arises predominantly from the divergence of the electron pressure tensor. Criteria based on the demagnetization of the electrons (large values of the electron agyrotropy and the Lorentz ratio) are found to characterize neither the immediate electron scale region around the X line nor the larger electron shear flow region.

Citation: Pritchett, P. L., and F. S. Mozer (2009), Asymmetric magnetic reconnection in the presence of a guide field, *J. Geophys. Res.*, *114*, A11210, doi:10.1029/2009JA014343.

1. Introduction

[2] Magnetic reconnection is typically identified in terms of large-scale phenomena involving particle energization, high-speed plasma flows, distinctive magnetic field patterns, and correlations between these effects such as the Walén relation [*Walén*, 1944; *Sonnerup et al.*, 1987]. From a fundamental perspective, the physics responsible for these macroscopic effects is controlled by a narrow boundary layer (the dissipation region) where dissipative processes allow the magnetic field to change topology. The configuration assumed in most kinetic studies of this region involves a symmetric region with a current sheet in the center bounded by antiparallel magnetic fields with equal asymptotic magnitudes and symmetric inflows of electrons and ions perpendicular to the magnetic field and particle outflows along the field lines. Such a symmetric treatment of the diffusion region has proved to be highly successful in understanding the basic kinetic features of magnetic reconnection [e.g., *Birn and Priest*, 2007]. This symmetric approach is well suited to tackling magnetotail reconnection where the presence of an average normal magnetic field component ensures that the plasma properties are nearly symmetric with respect to the midplane of the tail current sheet.

[3] At the magnetopause, however, there are several configurational aspects that destroy this symmetric setting for magnetic reconnection. Here, reconnection occurs between two topologically distinct regions, the shocked solar wind and the magnetosphere, which have quite different properties (plasma density, plasma temperature, and magnetic field strength). In addition, magnetopause reconnection is a persistent process that typically is directly driven by the solar wind. This adds an additional element of asymmetry to magnetopause reconnection.

[4] Until recently, most fully kinetic studies of magnetopause reconnection have not considered the influence of these asymmetries. Thus, most particle-in-cell (PIC) simulation studies motivated by the magnetopause have simply superimposed a uniform guide field on the symmetric Harris [*Harris*, 1962] current sheet [e.g. *Scholer et al.*, 2003; *Pritchett and Coroniti*, 2004; *Ricci et al.*, 2004; *Hesse et al.*, 2004; *Karimabadi et al.*, 2005a, 2005b; *Drake et al.*, 2006] and have typically employed periodic boundary conditions along the reversing field and/or assumed a large initial X line perturbation that forces the collapse of the current sheet from within. Early attempts to include the plasma and magnetic field asymmetries across the current layer included the Darwin PIC simulations of *Ding et al.* [1992] and the full electromagnetic PIC simulations of

[1]Department of Physics and Astronomy, University of California, Los Angeles, California, USA.
[2]Space Sciences Laboratory, University of California, Berkeley, California, USA.

Copyright 2009 by the American Geophysical Union.
0148-0227/09/2009JA014343$09.00

Swisdak et al. [2003]. In more recent PIC simulations, *Pritchett* [2008] used a hydromagnetic equilibrium including the effects of magnetic field and density gradients to study aspects of driven asymmetric reconnection in an open system without a guide field, *Tanaka et al.* [2008] examined the effects of density and temperature asymmetries on reconnection for the case of equal asymptotic magnetic field strengths, and *Huang et al.* [2008] explored the production of Debye-length scale electric fields associated with reconnection in a very thin (half width = $\rho_i/6$) magnetopause current sheet with asymmetric plasma density and temperature.

[5] In the present work, we extend the PIC model of *Pritchett* [2008] to include the case of driven asymmetric reconnection with a guide field. The guide field is an essential feature of the normal magnetopause configuration. As before, the initial configuration has a jump by a factor of three in the asymptotic strength of the reversing magnetic field from the magnetosheath to the magnetosphere sides of the current layer. Now a uniform guide field with strength equal to the magnetosheath reversing field is included, and the density decrease from the magnetosheath to the magnetosphere is a factor of ten. The magnetic shear angle across the current sheet is then 117°. The presence of the guide field destroys the north-south symmetry of the reconnection configuration. The resulting in-plane Hall currents lead to substantial enhancement of the out-of-plane (B_y) magnetic field inside the magnetic island on one side of the X line (northward (southward) for a dawnward (duskward) directed guide field) and a substantial reduction on the other side. The region of enhanced $|B_y|$ features a bipolar pair of $E_\parallel$ fields and an electron velocity flow shear layer, both extending several ion inertia lengths in the outflow direction out from the X line. The electron shear layer is observed to emit a train of small-scale (much less than the ion inertia length d_i) electron vortices which produce reductions of $\sim$30% in the ambient B_y field. No such shear layer or vortices occur in the opposite magnetic island. The Ohm's law $(\mathbf{E} + \mathbf{U}_e \times \mathbf{B}/c)_y = 0$ is found to be violated both in the immediate vicinity of the X line (where the violation is associated with both a nonzero divergence of the electron pressure tensor and nonzero convective derivatives of the electron flow velocity) and in the extended region of the electron shear flow layer (where the violation is associated almost entirely with the divergence of the electron pressure tensor). Criteria based on the concept of electron demagnetization [*Scudder et al.*, 2008], such as large values of the electron agyrotropy and the Lorentz ratio, do not serve to identify either the immediate electron scale region around the X line or the extended electron shear flow region.

[6] The outline of the paper is as follows. Section 2 describes the PIC simulation model including boundary conditions and the initial asymmetric hydromagnetic equilibrium configuration. Section 3 presents the simulation results. Section 3.1 examines the motion of the null line under one-sided driving and the reconnection rate. Section 3.2 documents the structure of the magnetic and electric fields in the reconnection configuration, examines the role of the Hall currents in establishing the north-south asymmetry, and identifies an electron velocity shear flow layer on one side of the X line. Section 3.3 discusses the role of the electron pressure divergence and inertial terms in producing violations of the ideal Ohm's law and considers the ability of various criteria associated with electron demagnetization to identify the reconnection site. Section 3.4 examines the production of small-scale electron vortices in the velocity shear layer. Section 4 presents data from a THEMIS magnetopause crossing that exhibit large-amplitude, short-duration magnetic field perturbations and $\mathbf{E} \times \mathbf{B}$ drifts that are consistent with the properties of the electron vortices observed in the simulation. Section 5 contains the summary and discussion.

2. Simulation Model and Configuration

[7] With a few exceptions to be noted below, the PIC simulation model and initial current sheet configuration are the same as employed in our previous investigation of asymmetric reconnection [*Pritchett*, 2008]. The current sheet structure is obtained from a hydromagnetic equilibrium in which the reversing magnetic field is given by

$$B_{0z}(x) = B_0[\tanh(x/\lambda) + R] \tag{1}$$

and the density profile by

$$n(x) = n_0\left[1 - \alpha\tanh(x/\lambda) - \alpha\tanh^2(x/\lambda)\right]. \tag{2}$$

The pressure balance constraint is satisfied if $R = 1/2$ and $\alpha n_0(T_i + T_e) = B_0^2/8\pi$. In the present study we choose $T_i = 2T_e$, $\alpha = 0.45$, and $T_i = 0.74B_0^2/4\pi n_0 \equiv 0.74 m_i v_A^2$. This gives a variation in magnetic field from $-B_0/2$ to $3B_0/2$ across the layer and a density variation from n_0 to $n_0/10$ (as opposed to a variation from n_0 to $n_0/3$ in the work of *Pritchett* [2008]). In addition, a uniform guide field $B_{0y} = B_0/2$ directed dawnward will be included. This results in a net ion beta value in the magnetosheath of $\beta_{i,sh} = 3.0$.

[8] This initial configuration is not a kinetic (Vlasov) equilibrium. To load the particle populations in the simulation, we assume drifting Maxwellian distributions for the electrons and ions with equal density $n(x)$ given by (2), with the drifts satisfying $U_{ey}/U_{iy} = -T_e/T_i$, and with the ion drift $U_{iy} = -[cB_0T_i/4\pi e\lambda(T_i + T_e)]\,[\mathrm{sech}^2(x/\lambda)]/n(x)$. We find then that the general structure of the current layer is well preserved on average when loaded into the particle simulation. The alterations do become more pronounced as the value of λ is decreased to the ion inertia length $d_i \equiv c/\omega_{pi}$ (ω_{pi} is defined using the magnetosheath density n_0) and below. Figure 1 presents profiles in x averaged over all values of z for $\lambda = 3d_i/2$, d_i, and $d_i/2$ computed from initial-value PIC simulations at a time $\Omega_{i0}t = 20$, which is well before any significant reconnection has occurred. The magnetic field B_z (Figure 1a) and density (Figure 1b) profiles are altered only slightly from those given in (1) and (2) [*Pritchett*, 2008]. As λ is decreased to d_i and below, a polarization electric field E_x (Figure 1c) develops on the magnetospheric side of the layer. As discussed by *Pritchett* [2008], this field is necessary to maintain charge neutrality between and pressure balance among the ions and electrons in the presence of the strong pressure gradient. In addition, as λ is decreased below d_i, the current density near $x = 0$ comes to be dominated by the electrons (Figures 1d and 1e) despite their lower temperature. In the present study, we will

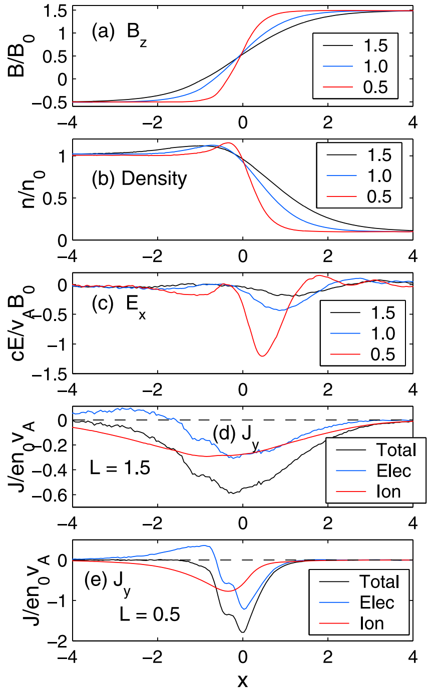

Figure 1. Profiles in x averaged over all values of z as determined from initial-value PIC simulations at time $\Omega_{i0}t = 20$: (a) magnetic field $B_z(x)$ for values of the half-thickness $\lambda = 1.5d_i$ (black curve), $\lambda = d_i$ (blue curve), and $\lambda = 0.5d_i$ (red curve), (b) same as Figure 1a but for the density $n(x)$, (c) same as Figure 1a but for the electric field $E_x(x)$, (d) electron (blue curve), ion (red curve), and total (black curve) current density $J_y(x)$ in a current sheet with initial half-thickness of $1.5d_i$, and (e) same as Figure 1d but for an initial half-thickness of $0.5d_i$.

start with a half-thickness $\lambda = d_i$, and the structure below the d_i scale will then develop self-consistently in response to the reconnection. In addition to the average changes in these x profiles, there are also some coherent bulk oscillations in the x direction with peak speed $\sim 0.01-0.02v_A$ for all three values of λ. These relatively small flows are soon masked by the development of the much larger reconnection flows.

[9] The present simulations employ a driving boundary condition at the magnetosheath x boundary only (*Pritchett* [2008] applied the external driving field at both x boundaries), and no local X line perturbation is applied at the center of the current sheet. The X line develops self-consistently in response to the driving field. This driving field has the form $E_{0y}(z) = E_{0y}\,\mathrm{sech}^2(z/D_z)$, where $cE_{0y}/v_AB_0 = 0.2$ and $D_z = 3.2d_i$. At the magnetosphere x boundary, conducting boundary conditions are assumed. The z boundaries are "open" [*Pritchett and Coroniti*, 1998, 2004] in that particles and magnetic flux are allowed to escape through these boundaries. Particles crossing a z boundary are removed from the system, and new particles are injected at a constant rate based upon the initial thermal Maxwellian distributions. In order to allow magnetic flux to escape, the perturbed field $\delta B_x \equiv 0$ at the boundary, corresponding to a zero-slope condition on the vector potential δA_y. In addition, it was found to be necessary to impose the condition $\delta B_y \equiv 0$ at the boundary in order to prevent the initial guide field from leaking out of the system. (Because of the high Alfvén speed in the magnetosphere side of the layer, the leakage occurred much more rapidly there than in the magnetosheath.) These conditions on δB_x and δB_y do not allow magnetic field perturbations to escape from the system, and the simulation must be stopped once these perturbations approach a z boundary.

[10] The present simulations use a $N_x \times N_z = 1024 \times 1024$ spatial grid corresponding to a system size $L_x \times L_z = 25.6d_i \times 25.6\,d_i$ with $d_i = 40\Delta$ (Δ is the uniform grid spacing). The ion to electron mass ratio is $m_i/m_e = 200$, $c/v_A = 20$, the electron Debye length $\lambda_{De} = 1.2\Delta$, and the time step is $\Omega_{e0}\Delta t = 0.1$. The magnetosheath density n_0 is represented by 420 particles per cell per species, and the total number of particles is 560 million. The coordinate system used in the simulations has x directed from the magnetosheath side toward the magnetosphere side of the current layer, y is directed dawnward, and z is directed northward. The results of the simulations will be presented using a set of dimensionless variables in which the magnetic field is normalized by B_0 (the average of the asymptotic values of the reversing magnetic field magnitudes on the magnetosheath and magnetosphere sides of the current layer), density is normalized to the magnetosheath density n_0, length is normalized to the ion inertia length c/ω_{pi} in the magnetosheath, time is normalized to the inverse ion cyclotron frequency Ω_{i0}^{-1} based on the field B_0, velocity is normalized to the Alfvén speed based on B_0 and n_0, electric field is normalized to v_AB_0, and current density to en_0v_A where e is the magnitude of the electron charge. If one chooses representative values of B_0 = 45nT and n_0 = 10 cm^{-3}, then the unit length is 72 km, the unit time is 0.23 s, the unit velocity is 311 km/s, and the unit electric field is 14 mV/m.

3. Simulation Results

3.1. Motion of the Magnetic X Line and the Reconnection Rate

[11] The previous driven simulation of *Pritchett* [2008] without a guide field and with driving from both x boundaries exhibited an appreciable delay as the driving E_y field propagated in from the boundaries. After this initial delay, a period of quasi-steady reconnection ensued with a normalized reconnection rate of $\tilde{E}_R \sim 0.10$, where $\tilde{E}_R$ was computed using the *Cassak and Shay* [2007] scaling relation that accounts for the different upstream values of the magnetic field and plasma density. In the present simulation with driving only from the magnetosheath boundary and the addition of a guide field, the overall time evolution is similar but with some important differences. Since flux is added only from one boundary, the location of the null in $B_z(x)$ moves inward toward the magnetosphere as a function of time, from the initial value of $x = -0.55d_i$ to $x \sim 1.2d_i$ at time $\Omega_{i0}t \sim 80$. In addition, the X line is shifted southward by about $2d_i$ relative to the maximum at $z = 0$ of the driving electric field on the boundary. This shift occurs in the direction of the electron diamagnetic drift for current sheets with a pressure gradient across the current layer in the presence of a guide field [*Swisdak et al.*, 2003; *Pritchett*, 2008].

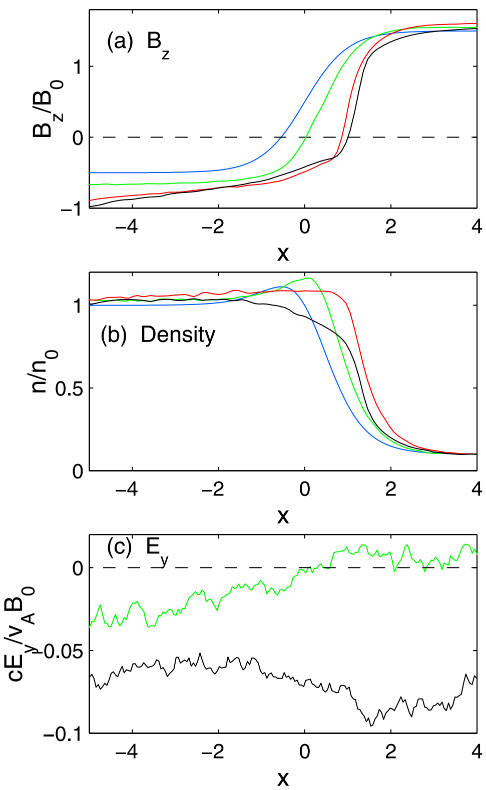

Figure 2. Profiles in x at fixed values of z at various times for (a) the magnetic field B_z, (b) the density, and (c) the electric field E_y. The blue curves are at time $\Omega_{i0}t = 0$ and at $z = 0$, the green curves are at $\Omega_{i0}t = 40$ and at $z = 0$, the red curves are at time $\Omega_{i0}t = 60$ and at $z = d_i$, and the black curves are at time $\Omega_{i0}t = 70$ and at $z = 2d_i$.

[12] The shift in the null of B_z is illustrated in Figure 2a, which shows the profile of $B_z(x)$ at times $\Omega_{i0}t = 0$ (blue curve, $z = 0$), $\Omega_{i0}t = 40$ (green curve, $z = 0$), $\Omega_{i0}t = 60$ (red curve, $z = -d_i$), and $\Omega_{i0}t = 70$ (black curve, $z = -2d_i$). In addition to the shift, the slope of the profile increases, corresponding to the increase in the $|J_y|$ current density. Figure 2b shows the corresponding density profiles, indicating that the density gradient increases with time. Figure 2c shows the E_y profile at times $\Omega_{i0}t = 40$ and $\Omega_{i0}t = 70$; these profiles are averaged over a time interval of $0.25\Omega_{i0}^{-1}$. At the earlier time, the inductive field has not yet penetrated all the way in from the magnetosheath to the null, and the corresponding reconnection rate is essentially zero. At the later time, the reconnection field $|E_y|$ is enhanced in the vicinity of the null with $c|E_y|/v_A B_0 \sim 0.08$. Since the inflow into the X line is almost entirely from the sheath side, the appropriate upstream conditions are those on the magnetosheath side. Here the density is n_0, and the field strength $|B_z| \sim 0.8\ B_0$. Thus an appropriately normalized reconnection rate is $\tilde{E}_R \sim cE_y/v_A B_0(0.8)^2 \sim 0.12$.

3.2. Magnetic and Electric Field Structure

[13] We initially consider the structure of the reconnection fields at $\Omega_{i0}t = 70$ at which time the reconnection is well established. Figure 3 shows the x, y, z components and the total magnitude of the magnetic field at this time; superimposed in each plot are the in-plane projections of the magnetic field lines. As has already been noted, the X line has shifted southward by about $2d_i$ relative to the maximum at $z = 0$ of the driving electric field on the boundary. The reconnected magnetic field B_x (Figure 3a) is not constant as a function of x but is enhanced in magnitude at the magnetosheath separatrix. As a consequence, it is inappropriate to perform a minimum variance analysis to transform space data to the coordinate system of the current sheet for asymmetric reconnection since this forces B_x to be essentially constant [*Mozer and Retinò*, 2007; *Mozer et al.*, 2008]. The B_z field (Figure 3c) in the magnetosheath has been enhanced in magnitude by somewhat less than a factor of two from the initial value as a result of the addition of flux from the boundary. There is a further small increase in magnitude at the magnetosheath separatrix.

[14] The structure of the out-of-plane component B_y (Figure 3b) proves to be quite significant for the future discussion. In the northern outflow region, the B_y field is substantially increased, with a maximum of $\sim 0.9B_0$ being achieved just inside the magnetosheath separatrix. In contrast, in the southern outflow region, the B_y magnitude is substantially reduced, and the field even changes sign in a small region inside the magnetosheath separatrix. (If the guide field was initially directed duskward instead of dawnward, the roles of the north and south outflow regions would be switched.) This structure of the B_y field arises from the strong in-plane Hall currents that exist in the reconnection configuration. Figure 4 shows the z component of the bulk ion and electron flow velocities as well as the resulting J_z current density. The ion outflow in the northern hemisphere peaks along the magnetosphere separatrix and extends on either side into the right half of the island and into the magnetosphere, while in the southern hemisphere the outflow is somewhat weaker and tends to fill the entire island. In contrast, the electron flows are strongly concentrated along the separatrices, representing a flow of the electrons from the high-density to the low-density side of the layer. Since the electron flows are much larger, they mainly determine the current density. These Hall currents reinforce the B_y field just inside the northern magnetosheath separatrix (and to a lesser degree just inside the northern magnetosphere separatrix), while in the southern hemisphere the B_y field is reduced in magnitude (and even reversed). In addition to the electron flows on the separatrices, there is also a distinct outflow in the center of the northern island that extends several d_i away from the X line as well as a somewhat weaker return flow situated adjacent to the outflow on the magnetosphere side. These electron flows constitute a velocity shear layer, which is discussed further in sections 3.3 and 3.4. The current density produced by the shear layer tends to weaken the B_y field in the immediate vicinity of the X line.

[15] Figure 5 shows the x, y, z, and parallel components of the electric field at time $\Omega_{i0}t = 70$. These fields are dominated by the strong magnetosheath-directed E_x component. The strength $cE_x/v_A B_0 \sim 3$ or about 40mV/m in physical units. This field plays the role of opposing the ion inflow from the magnetosheath and maintaining charge neutrality with the much less dense population of magnetosphere electrons. The other electric field components are

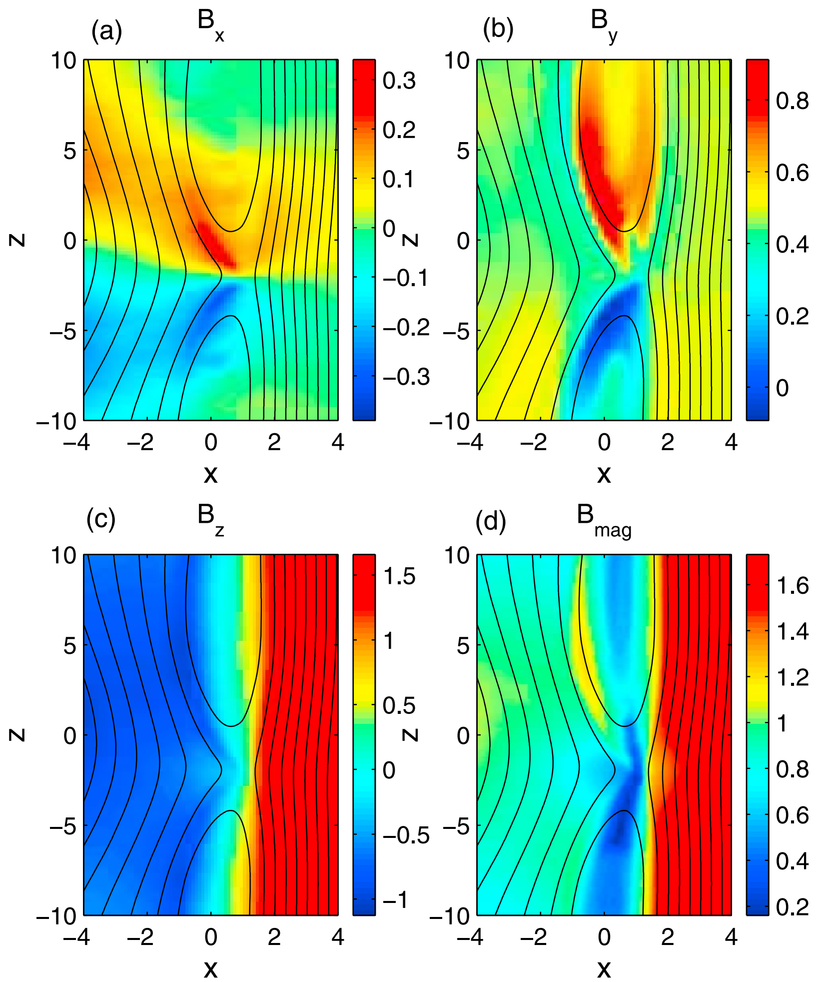

Figure 3. Structure of the magnetic field components at time $\Omega_{i0}t = 70$: (a) B_x, (b) B_y, (c) B_z, and (d) the magnitude B_{mag}.

much weaker. The reconnection E_y field is the weakest and is relatively uniform over the whole island region. This is similar to the structure observed for the case of symmetric reconnection [e.g., *Pritchett*, 2001]. The E_z field is located mainly along the separatrices, while $E_{\|}$ exhibits two sets of bipolar fields: a stronger pair close to the X line and a weaker pair in the region of the electron velocity shear layer northward of the X line.

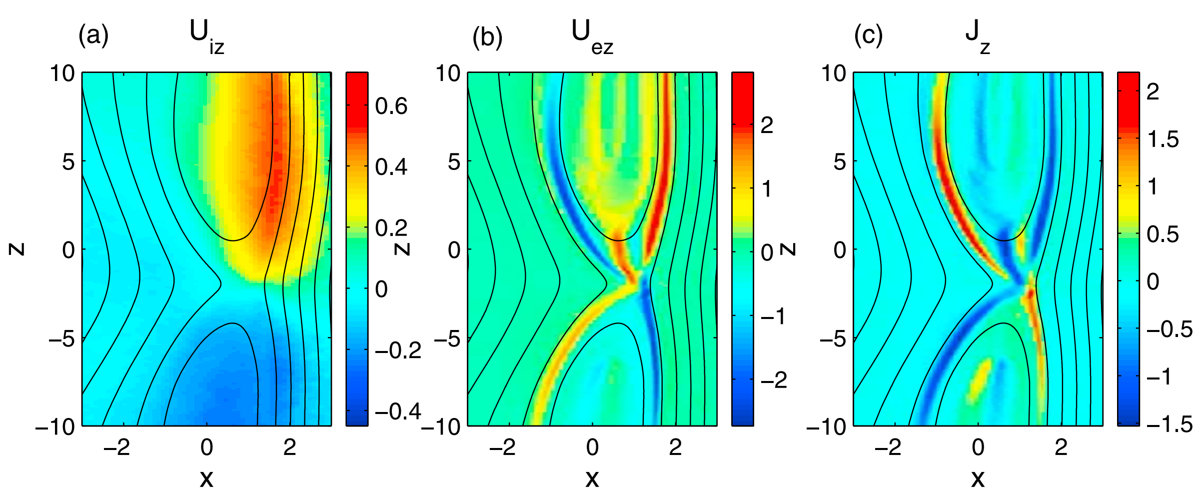

Figure 4. Structure at time $\Omega_{i0}t = 70$ of (a) the ion flow velocity U_{iz}, (b) the electron flow velocity U_{ez}, and (c) the current density J_z.

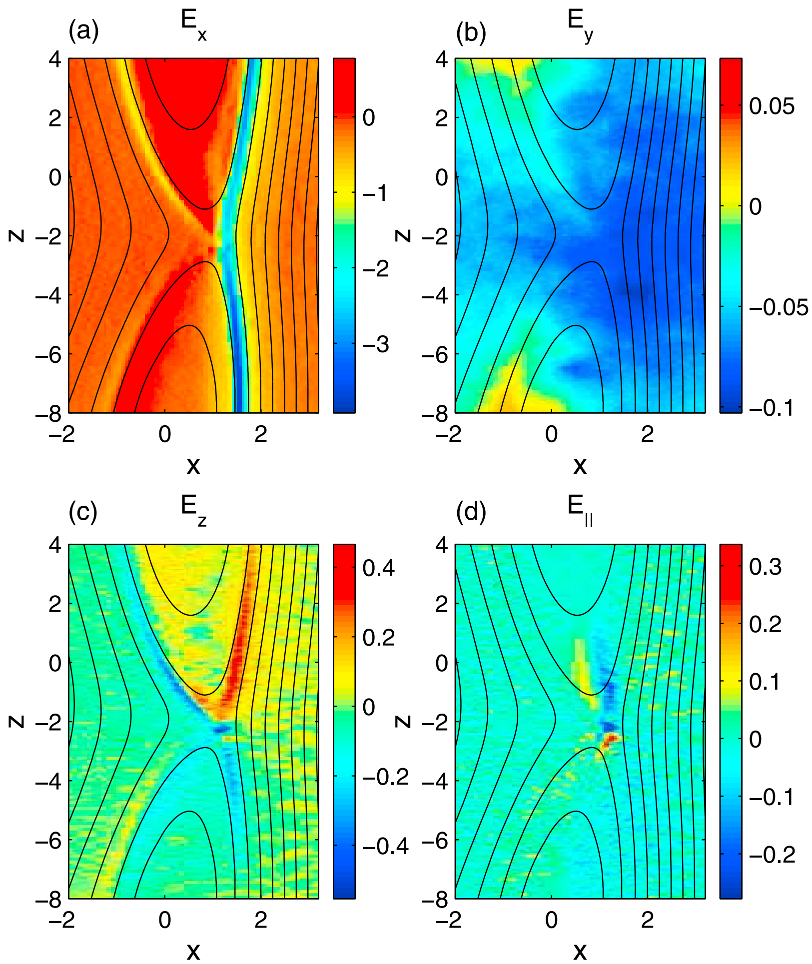

Figure 5. Structure of the electric field components at time $\Omega_{i0}t = 70$: (a) E_x, (b) E_y, (c) E_z, and (d) the parallel field $E_{\|}$.

[16] In addition to the large negative E_x field along the magnetosphere separatrix, there is a weaker positive E_x field extending northward from the X line and filling the magnetosheath side of the island. Thus the electron velocity shear layer is bounded by a positive E_x on the left side and a negative E_x on the right side. The resulting $E_x \times B_y$ drift accounts for the origin of the shear layer. In contrast, no shear layer exists in the southern portion of the island since the B_y field is nearly zero there.

3.3. Ohm's Law and Electron Demagnetization

[17] The generalized Ohm's law for a two-fluid (electron and ion) system follows directly from the electron momentum equation and can be written in the alternative forms

$$\mathbf{E} + (\mathbf{U}_e \times \mathbf{B})/c = -(\nabla \cdot \underline{\mathbf{P}}_e)/en - (m_e/e) \cdot [\partial \mathbf{U}_e/\partial t + (\mathbf{U}_e \cdot \nabla)\mathbf{U}_e], \quad (3)$$

$$\mathbf{E} + (\mathbf{U}_i \times \mathbf{B})/c = (\mathbf{J} \times \mathbf{B})/enc - (\nabla \cdot \underline{\mathbf{P}}_e)/en - (m_e/e) \cdot [\partial \mathbf{U}_e/\partial t + (\mathbf{U}_e \cdot \nabla)\mathbf{U}_e]. \quad (4)$$

Here, $\underline{\mathbf{P}}_e$ is the electron pressure tensor, and $\mathbf{U}_e$ ($\mathbf{U}_i$) is the bulk electron (ion) flow velocity. The left hand sides of these two equations are frequently referred to as the "frozen-in" conditions for the electrons and ions, respectively; they differ by the Hall term $(\mathbf{J} \times \mathbf{B})/enc$. Figure 6 shows the x, y, z components of the left-hand side for the electrons and ions. These results for the Ohm's law were discussed previously by *Mozer and Pritchett* [2009]; they are repeated here in order to present a self-contained discussion of asymmetric reconnection and to facilitate discussion of some additional properties of the Ohm's law. (Note that in the work of *Mozer and Pritchett* [2009] the color scales were saturated at half of the maximum absolute value. In the plots in Figure 6 the full dynamic range is preserved in the color scales.) The x component is large in magnitude for both species along the entire magnetosphere separatrix, while the signs are opposite, reflecting the large value of $U_{ey}B_z$ and the dominant electron contribution to the J_y current density associated with the gradient in B_z. Significant nonzero values of $(\mathbf{E} + \mathbf{U}_e \times \mathbf{B}/c)_y$ are not confined to the immediate vicinity of the X line but also extend several d_i northward in the region of the electron shear layer. This violation of the electron Ohm's law is analogous to the existence of the electron outflow jets that have been observed to extend over scales of tens of d_i in symmetric reconnection configurations in both PIC simulations [*Karimabadi et al.*, 2007; *Shay et al.*, 2007] and in observations [*Phan et al.*, 2007]. The region where the y component of the electron Ohm's law is nonzero in the

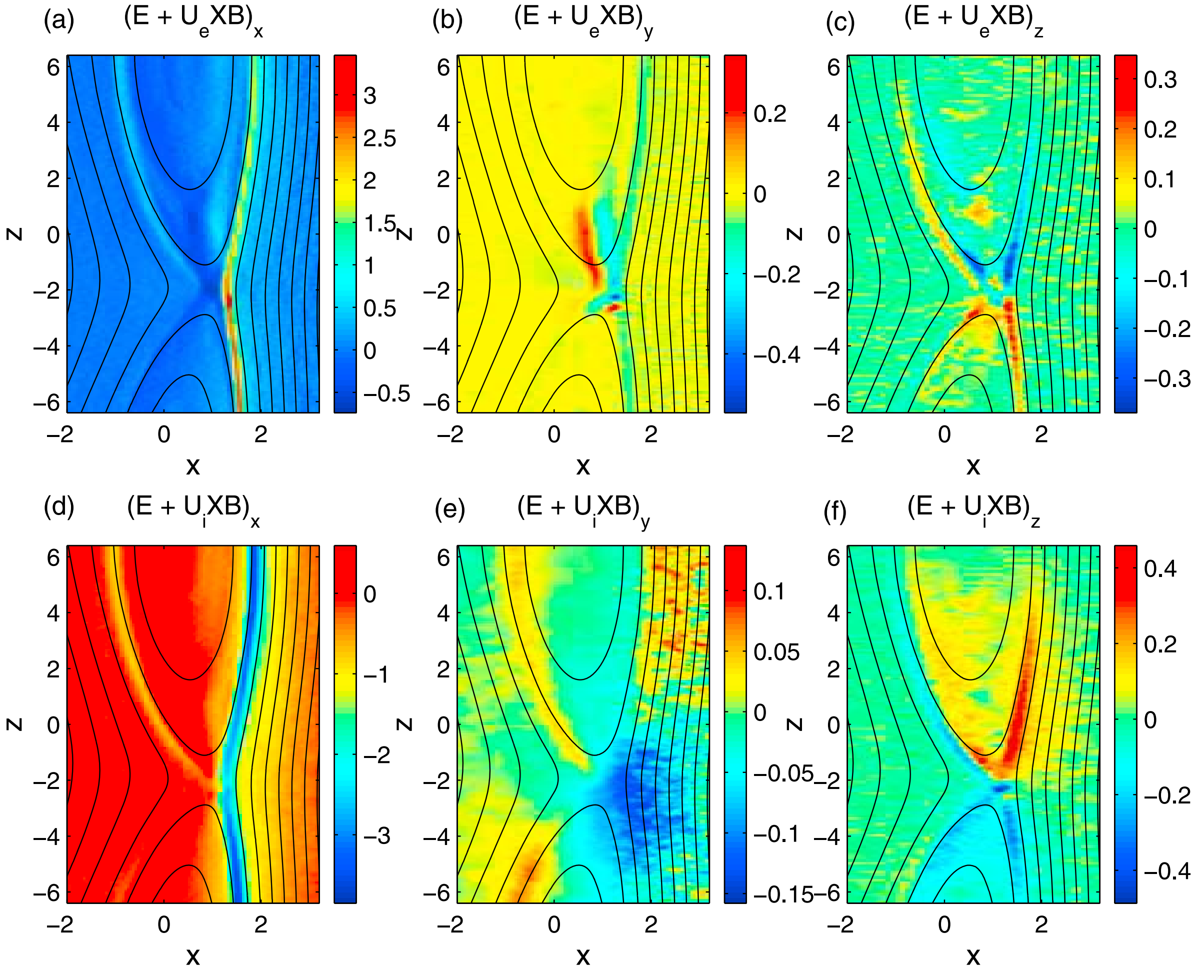

Figure 6. Structure at time $\Omega_{i0}t$ = 70 of the ideal Ohm's law expression $\mathbf{E} + (\mathbf{U} \times \mathbf{B})/c$ for (a) the electron x component, (b) the electron y component, (c) the electron z component, (d) the ion x component, (e) the ion y component, and (f) the ion z component.

present results is not entirely contained within the region where the corresponding component of the ion Ohm's law is nonzero [*Mozer and Pritchett*, 2009].

[18] The x, y, z components of the divergence of the electron pressure tensor and of the convective derivative $(\mathbf{U}_e \cdot \nabla)\mathbf{U}_e$ were presented in Figure 4 of *Mozer and Pritchett* [2009]. There it was shown that the two sides of the x component of (3) and (4) match very closely and that the divergence of the electron pressure tensor term is dominated by the diagonal term $\partial P_{exx}\partial x$. Once this diagonal term is removed (it represents a polarization field whose curl vanishes), the peak magnitudes of the remaining electron divergence terms are typically larger by a factor of 2 or 3 than those of the inertial convective terms. However, the inertial terms are not negligible everywhere. In particular, for the y components in the immediate vicinity of the X line, the inertial and pressure divergence terms can be comparable. Thus at $x = 1.2$, $z = -2.7$ the pressure divergence and inertial contributions to the right-hand side of the Ohm's law are 0.17 and 0.20, respectively. Their sum matches the left-hand side value of $(\mathbf{E} + \mathbf{U}_e \times \mathbf{B}/c)_y = 0.35$. Only slightly away at $x = 1.3$, $z = -2.2$, the signs of the right-hand terms reverse, and the pressure-divergence and inertial contributions are -0.40 and -0.15, respectively. The left-hand side is -0.55. Thus the validity of the generalized Ohm's law is maintained in the simulation. In the electron velocity-shear region, however, the pressure divergence term is much larger than the inertial term, and the bipolar nature of the former closely matches that of $(\mathbf{E} + \mathbf{U}_e \times \mathbf{B}/c)_y$.

[19] The nonvanishing of the Ohm's law $(\mathbf{E} + \mathbf{U_e} \times \mathbf{B}/c)_y$ over distances extending several ion inertia lengths away from the X line (Figure 6b) indicates that the electron frozen-in condition is violated over much larger distances than is normally assumed. The question then arises as to whether there is some other quantity that identifies the X line region itself. Recently, *Scudder et al.* [2008] have argued that the key principle for locating the X line is the demagnetization of the electrons. This suggestion was supported by the results of 2D simulations of symmetric reconnection with and without a guide field [*Scudder and Daughton*, 2008]. Note that this usage of "demagnetization" refers specifically to the breaking of the frozen-in condition that enables reconnection as opposed to the simple lack of magnetized orbits that occurs near an X line in the absence of a guide field. Here we use the present asymmetric reconnection simulation results to determine whether the Scudder et al. demagnetization criteria are capable of marking the X line site.

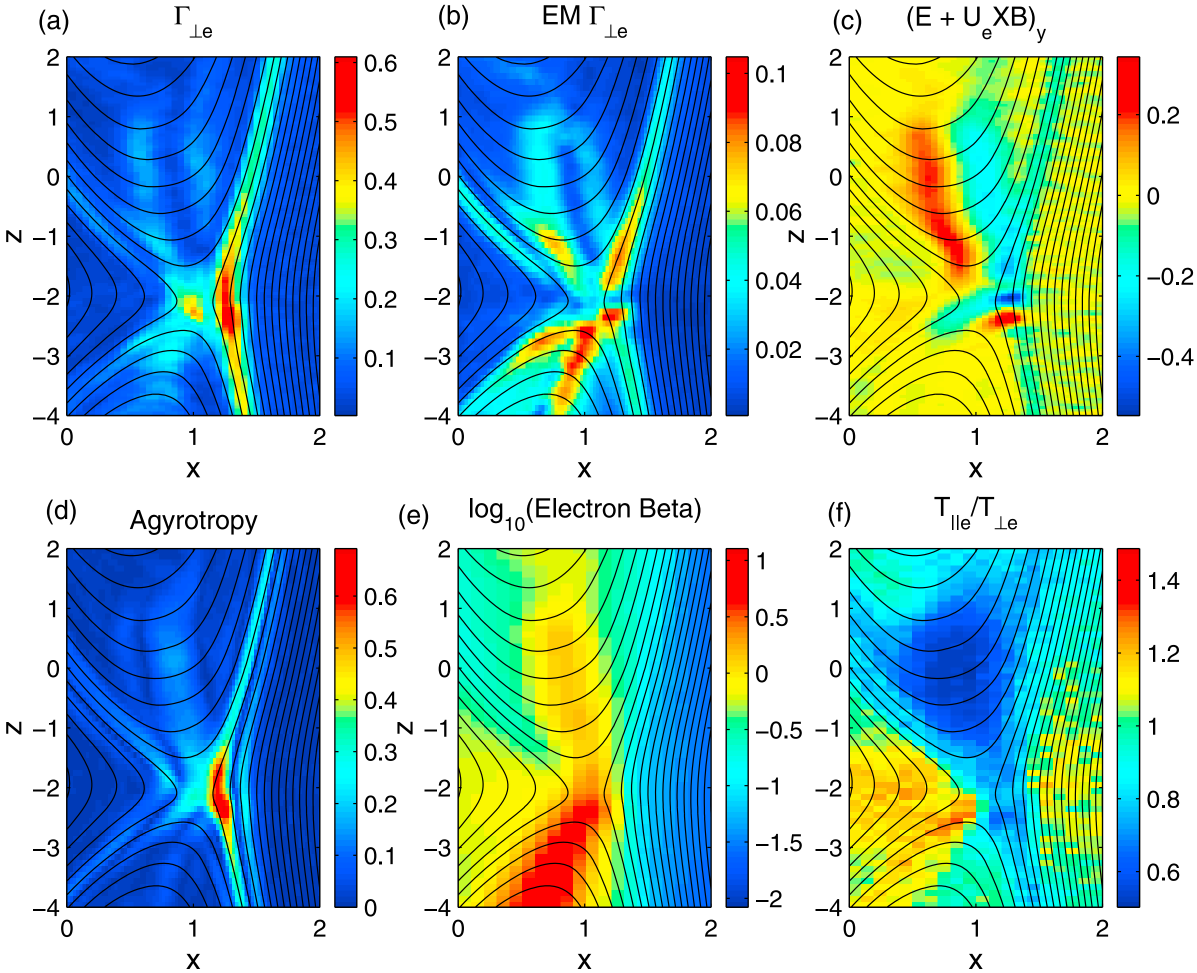

Figure 7. Structure at time $\Omega_{i0}t$ = 70 of (a) the electron Lorentz factor $\Gamma_{\perp,e}$, (b) the electromagnetic Lorentz factor $\tilde{\Gamma}_{\perp,e}$, (c) the ideal Ohm's law expression $(\mathbf{E} + \mathbf{U}_e \times \mathbf{B}/c)_y$, (d) the electron agyrotropy, (e) $\log_{10}$ of the electron beta, and (f) the temperature ratio $T_{\|}, e/T_{\perp,e}$.

[20] The demagnetization criteria cited by Scudder et al. are the electron agyrotropy and the ratio of the perpendicular electric to magnetic force experienced by a thermal speed electron in the electron fluid's rest frame (the Lorentz ratio). Agyrotropy is a scalar measure of the departure of the pressure tensor from cylindrical symmetry about the local magnetic field direction. The utility of agyrotropy as a diagnostic tool has been greatly augmented by the development of a fast algorithm [*Scudder and Daughton*, 2008] to evaluate the agyrotropy directly from the pressure tensor without the use of eigenvalue routines. The Lorentz factor is related to the adiabatic expansion parameter $\delta \equiv \rho_e/L$ (where ρ and L are the gyroradius and scale length of variation, respectively) and is given by

$$\Gamma_{\perp,e} = \sqrt{\pi}c|\mathbf{E}_\perp + \mathbf{U}_e \times \mathbf{B}/c|/w_{\perp e}B, \tag{5}$$

where $w_{\perp e} = (2kT_{\perp e}/m_e)^{1/2}$.

[21] Figures 7a, 7d, and 7e show the structure at $\Omega_{i0}t = 70$ of $\Gamma_{\perp},e$, the agyrotropy, and the electron beta, respectively. The region where $\beta_e \gg 1$, extending southward away from the X line and inside the magnetosheath separatrix, indicates a region where the electron orbits are relatively unmagnetized (B_y is nearly zero in this region). Along the magnetosphere separatrix and the northern magnetosheath separatrix $\beta_e \ll 1$. The $\Gamma_{\perp,e}$ factor is large primarily along the magnetosphere separatrix as a consequence of the large E_x that exists there. In addition, $\Gamma_{\perp,e}$ has a secondary maximum at the X line itself ($x \approx 1, z \approx -2$). In the high β_e region in the southern part of the island, $\Gamma_{\perp,e}$ is quite small. The large value of $\Gamma_{\perp,e}$ on the magnetosphere separatrix results from the large contribution of the diagonal component of the electron pressure tensor divergence $-(1/en)\partial P_{exx}/\partial x$ to $(\mathbf{E} + \mathbf{U}_e \times \mathbf{B}/c)_x$. This term has zero curl and thus does not break the frozen-in condition. To remove this contribution, we define an electromagnetic $\tilde{\Gamma}_{\perp,e}$ in which $(\mathbf{E} + \mathbf{U}_e \times \mathbf{B}/c)_x$ in the numerator of (5) is replaced by the off-diagonal term $-(1/en)\partial P_{exz}/\partial z$. This new quantity is plotted in Figure 7b. It peaks near the X line, but its magnitude there and elsewhere is very small, $\lesssim$0.1. The agyrotropy does become appreciable along the magnetosphere separatrix, reflecting the presence of the thin electron layer there, but this peak is shifted from the X line itself. Figure 7c repeats the plot of the Ohm's law $(\mathbf{E} + \mathbf{U_e} \times \mathbf{B}/c)_y$ but now for the present reduced area around the X line. This quantity clearly marks the electron shear region, while neither the $\Gamma_{\perp,e}$ quantities nor the agyrotropy exhibit significant values that would permit the identification of

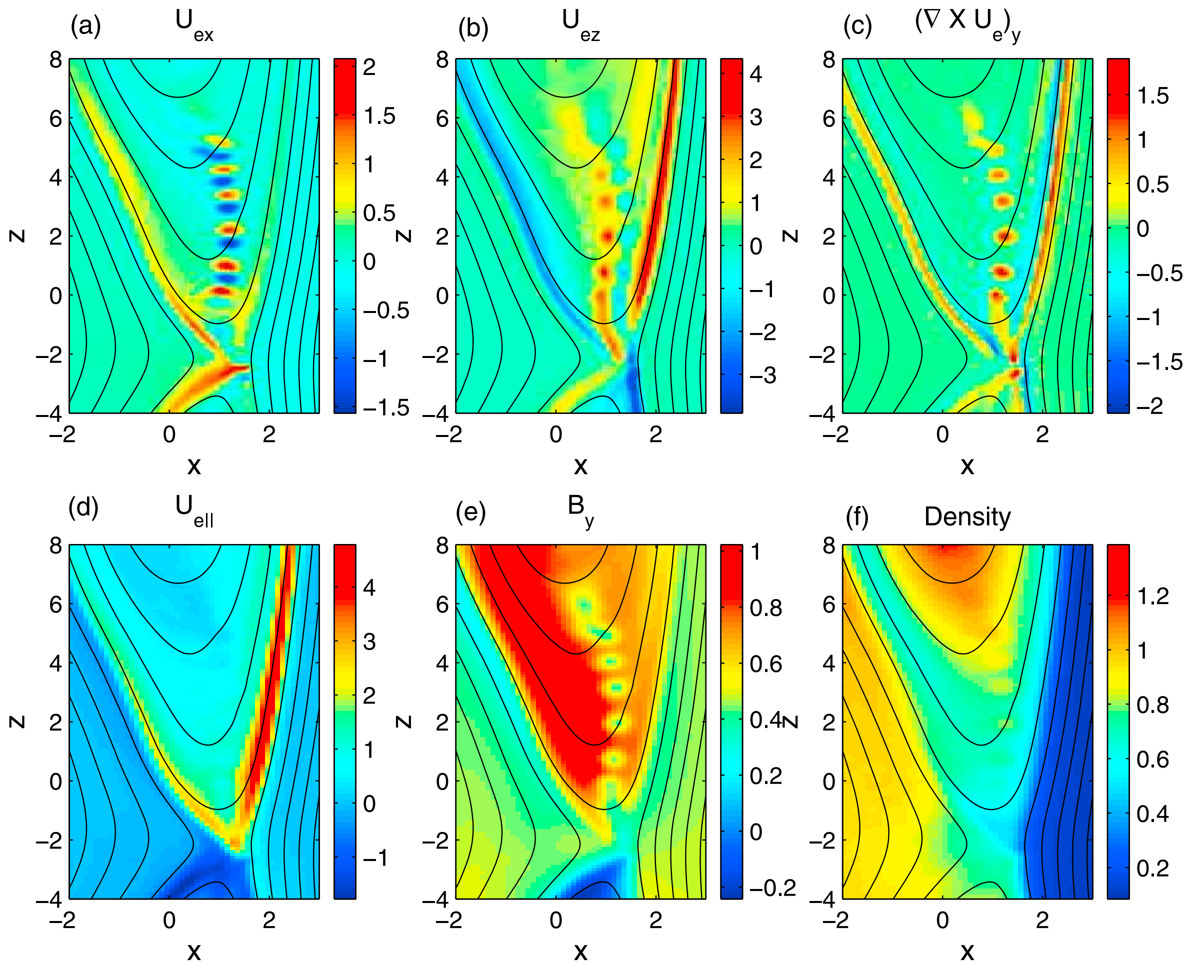

Figure 8. Structure at time $\Omega_{i0}t = 80$ of (a and b) the electron flow velocities U_{ex} and U_{ez}, (c) the y component of the electron vorticity $\nabla \times \mathbf{U}_e$, (d) the parallel component of the electron flow velocity $U_{e\|}$, (e) the magnetic field component B_y, and (f) the plasma density.

this region. Figure 7f shows that this region has an appreciable electron temperature anisotropy with $T_{\|,e} < T_{\perp,e}$.

[22] The present results thus indicate that the various parameters that have been associated with electron demagnetization do not in general achieve maxima of order unity within the small region of size $c/\omega_{pe} \times c/\omega_{pe}$ around the X line. They do achieve such values on the nearby portion of the magnetospheric separatrix, but they are relatively insensitive to the electron flow shear region where the frozen-in condition is violated over many ion inertia lengths as indicated by the nonvanishing of $(\mathbf{E} + \mathbf{U_e} \times \mathbf{B}/c)_y$. In a full 3D setting, however, the utility of this latter condition may be considerably reduced.

3.4. Small-Scale Electron Vortices

[23] As noted previously in Figures 4 and 6, there is an electron velocity shear flow layer extending northward from the X line. Classically, such a shear layer is unstable to the Kelvin-Helmholtz instability. Figures 8a and 8b show the U_{ex} and U_{ez} velocity flows at time $\Omega_{i0}t = 80$. There are clear alternating structures in both velocity components extending northward from the shear layer. Figure 8c shows the y component of the vorticity $\partial U_{ex}/\partial z - \partial U_{ez}/\partial x$ for these flows. It is evident from this plot that there is a series of clockwise rotating vortices (as viewed from above) emanating from the shear layer. The full width of the vortices is $\sim 0.3 d_i$, and their northward propagation speed is $\sim 0.3 v_A$. Figure 8d shows that the vortical flow produces essentially no signature in $U_{e\|}$; the main parallel flows are concentrated along the separatrices. The electron current density in the vortices is counterclockwise, and this produces a negative B_y perturbation (directed out of the page) which opposes the guide field inside the island. This produces a characteristic reduction of $\sim 30\%$ in the magnitude of the B_y field (Figure 8e). The perturbations in the density are considerably weaker (Figure 8f). Note that the smooth behavior of the magnetic field line projections in the region of the vortices in Figure 8 is somewhat deceptive. These projections are sensitive only to the in-plane magnetic field components and do not reflect the strong modulation of the B_y field. The actual behavior of a field line in 3D would be affected by the vortices. It is clear, however, that the magnetic field is not "frozen-in" to the electron vortices, and the region of nonzero $(\mathbf{E} + \mathbf{U}_e \times \mathbf{B}/c)_y$ shown in Figure 6b extends upward in z with the vortices, reaching to $z \approx 6d_i$ at $\Omega_{i0}t = 80$ and to $z \approx 8d_i$ at $\Omega_{i0}t = 85$. Thus the violation of the frozen-in condition for the electrons occurs in an elongated region of at least $10d_i$ in length.

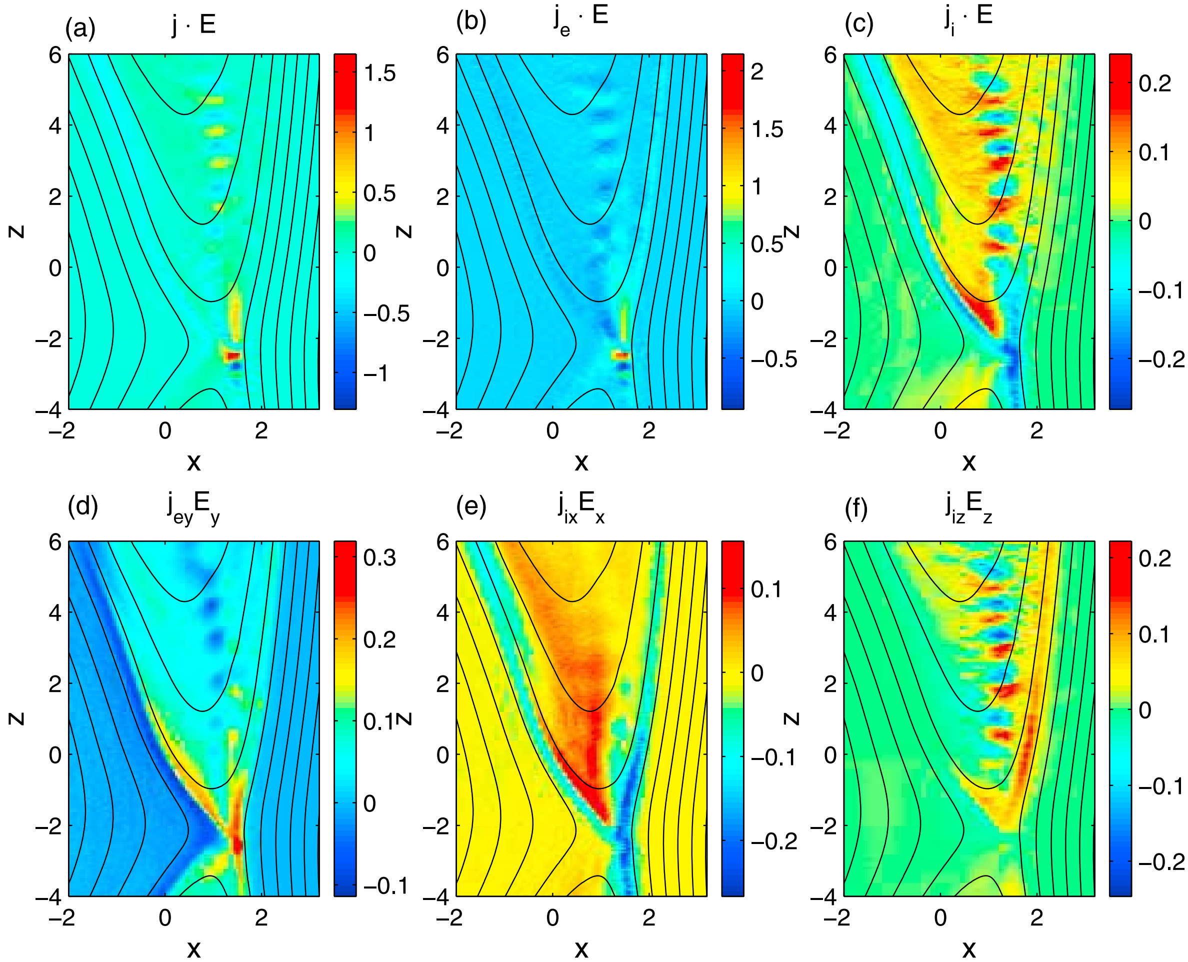

Figure 9. Structure at time $\Omega_{i0}t = 80$ of (a) the energy conversion $\mathbf{J} \cdot \mathbf{E}$, (b) the electron contribution $\mathbf{J}_e \cdot \mathbf{E}$, (c) the ion contribution $\mathbf{J}_i \cdot \mathbf{E}$, (d) the term $J_{ey}E_y$, (e) the term $J_{ix}E_x$, and (f) the term $J_{iz}E_z$.

[24] We now compare the properties of the electron vortices in the simulation with those predicted by the classical Kelvin-Helmholtz instability [e.g., *Miura and Pritchett*, 1982]. For a velocity shear profile of the form $U_z(x) = u_1 + u_2 \tanh(x/L_v)$, the fastest growing mode has wave number $k_z L_v = 0.45$ and a linear growth rate $\gamma_{\max} L_v/u_2 = 0.19$. The wavelength of the fastest growing mode is then $14L_v$. For the electron shear layer in Figure 4b near $x = 1$, $z = 0$, we find values $u_1/v_A = 0.55$, $u_2/v_A = 1.31$, and $L_v = 0.11d_i$. The predicted wavelength is then $1.5d_i$ and the growth rate is $2.3\Omega_{i0}^{-1}$. In Figure 8 ($\Omega_{i0}t = 80$) the largest spacing between vortices is $\sim 1.1d_i$, while at $\Omega_{i0}t = 85$ (data not shown), the largest spacing is $\sim 1.4d_i$. The development time of the vortices is $\sim 5\Omega_{i0}^{-1}$. Thus both the spacing and growth time are consistent with a Kelvin-Helmholtz origin for the vortices.

[25] Figure 9a shows the energy conversion term $\mathbf{J} \cdot \mathbf{E}$ at time $\Omega_{i0}t = 80$. Here $\mathbf{J} \cdot \mathbf{E}$ is evaluated in the simulation frame, which is the one (essentially) tied to the X line. This term is dominated by a large positive value in a small region near the X line and a slightly weaker negative value nearby. These structures are dominated by the electron U_{ex} flow (which has a positive value in along the separatrix toward the X line and a small localized region with negative value; see Figure 8a) interacting with the strong polarization field E_x. These large magnitudes of $\mathbf{J} \cdot \mathbf{E}$ are associated with the perpendicular current density and electric field; the parallel contribution $J_\parallel E_\parallel$ (not shown) is smaller by an order of magnitude and tends to maximize on the magnetosphere separatrix. In the vortex region there is a series of weaker alternating-sign structures in $\mathbf{J} \cdot \mathbf{E}$ propagating away from the X line. The northward propagation of these structures can be seen in Animation 1.[1] Figures 9b and 9c show the separate contributions of the electron and ion current densities to $\mathbf{J} \cdot \mathbf{E}$. While the electrons dominate the energy conversion near the X line, both species contribute to $\mathbf{J} \cdot \mathbf{E}$ in the vortex region. $J_{ey}E_y$ (Figure 9d) is considerably weaker in magnitude than the peak values of either $J_{ex}E_x$ or $J_{ez}E_z$, but it is uniformly positive in the X line region and negative in the vortex region. $J_{ix}E_x$ (Figure 9e) is positive in the left half of the island and negative along the magnetosphere separatrix where the ion inflow is stopped by the polarization E_x field. $J_{iz}E_z$ (Figure 9f) is positive along the outflow magnetosphere separatrix and has a pronounced alternation of sign in the vortex region.

4. Possible Observation of Electron Vortex Signatures

[26] The characteristic signatures of the electron vortices associated with asymmetric guide field reconnection are that

[1] Animation available in the HTML.

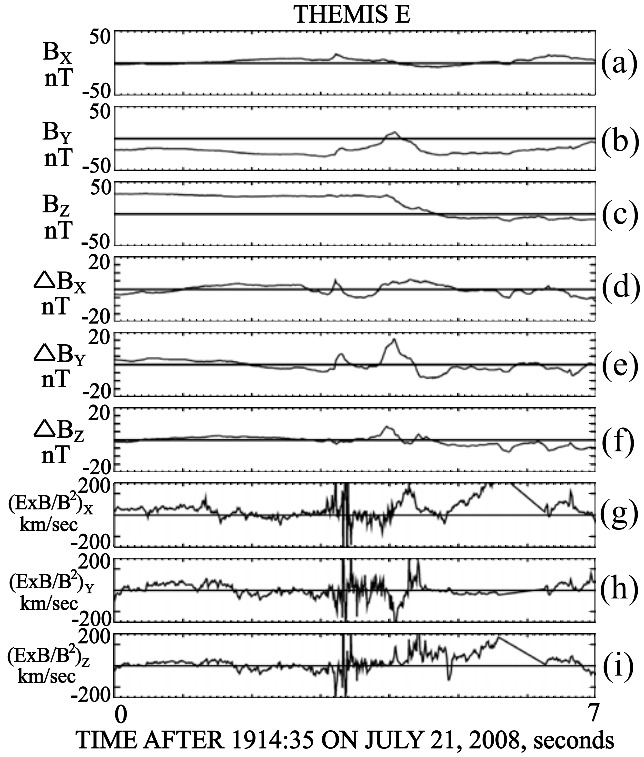

Figure 10. Magnetopause crossing by the THEMIS E spacecraft on 21 July 2008. (a–c) Magnetic field measured by the FGM instrument, (d–f) magnetic field deviations measured by the search-coil magnetometer, and (g–i) $\mathbf{E} \times \mathbf{B}/B^2$ drifts determined from electric and magnetic field measurements.

they occur over spatial scales of several electron inertial lengths (corresponding to $\sim$3–6 km) and they produce substantial reductions in the guide field magnitude of the order of 30–40%. For a spacecraft moving at $\sim$20 km/s, the encounter time will be $\sim$0.2 seconds. To attempt to identify such large field perturbations in the in situ data, one needs a spacecraft whose search coil magnetometers do not saturate at low levels. The THEMIS instrumentation [*Roux et al.*, 2008] includes magnetometers with such capabilities. The plasma flow measurements, however, do not have adequate time resolution to observe the vortical flows directly. Thus the following are the primary requirements for observing a possible vortex in the THEMIS data:

[27] 1. It occurs in the current sheet of a magnetopause crossing.

[28] 2. A large $|\Delta B_y|$ that is bigger than $|\Delta B_x|$ or $|\Delta B_z|$.

[29] 3. A sign of ΔB_y that reduces the magnitude of B_y.

[30] 4. A magnitude of ΔB_y that is $\sim$0.3–0.4B_0 or about 10–12 nT.

[31] 5. A duration $\sim$0.2s corresponding to traversal across a structure of size several c/ω_{pe}.

[32] Figure 10 shows data for a THEMIS magnetopause crossing on 21 July 2008 that satisfies these criteria. This event is unusual but not unique; it is one of three candidates found in searching nearly 200 magnetopause crossings by the THEMIS spacecraft E from June 2008 to November 2008. The total length of time plotted is 7s, and the spacecraft was traveling from the magnetosphere into the magnetosheath. After the end of the time interval in the plot, it passed all the way into the magnetosheath. Figures 10a–10c show the magnetic field components in the minimum variance coordinate system, which was selected over maximum variance or joint variance rotations because it produced the rotation matrix closest to a unit matrix, as would be expected for rotation from the GSE coordinate system for a subsolar magnetopause crossing. The magnetopause crossing is evidenced in the B_z trace in Figure 10c. Note, however, that a significant portion of the drop in the magnitude of B is associated with the change in B_y; thus this does not look like a classical crossing but instead has a twisted structure with a large current component in the x or z directions. Figures 10d–10f show the search-coil magnetometer results for the magnetic field perturbations. The largest B_y perturbation near 19:14:39 is about three times as large as those in B_x and B_z and it reduces the magnitude of B_y (and even drives B_y to the opposite sign). The full-width-at-half-maximum duration of the main B_y pulse is 0.3 seconds. Figures 10g–10i show the components of $\mathbf{E} \times \mathbf{B}/B^2$. While there are considerable fluctuations in this data, there are also coherent structures around the time of the crossing at 19:14:39. Thus there is a unipolar structure in the x component reaching up to $\sim$200 km/s which coincides with a bipolar structure in the y component which varies between $\sim\pm$200 km/s. The z component becomes uniformly positive during the latter part of this time interval.

[33] Figures 11a, 11b, and 11c show the $-x$, $-y$, and z components, respectively, of $c(\mathbf{E} \times \mathbf{B})/B^2$ from the simulation at time $\Omega_{i0}t = 80$. (The x and y components have their signs reversed in order to facilitate a direct comparison with the THEMIS data in Figure 10 which are expressed in GSM coordinates.) This fluid drift is not a quantitatively accurate representation of the actual electron flows (see Figure 8), but is presented for comparison with the THEMIS data. The large $E \times B$ flow in the y direction along the magnetosphere separatrix is clearly not present in the THEMIS data; this is an indication that the THEMIS crossing is not a "classical" one. For the small scale flows that could be indicative of the vortices, the comparison is much better. Figure 11d shows cuts of $(\mathbf{E} \times \mathbf{B})_x$ along the lines $z = 0.6$ (blue line) and 1.6 (red line) which pass through two of the magnetosheath-flowing edges of the vortices. In agreement with the THEMIS data, this flow has a single sign, and the peak magnitudes correspond to 120–210 km/s. Figure 11e shows similar cuts for $(\mathbf{E} \times \mathbf{B})_y$. The large negative drift along the magnetosphere separatrix occurs at $x \approx 2$. As one continues into the island from the magnetosphere side, the $-y$ drift experiences a negative maximum and then a positive excursion. This occurs over the same spatial range where the $-x$ drift is positive. The magnitudes of the $-y$ drifts are comparable to the THEMIS values. Figure 11f shows the z drift. This also changes sign, and the magnitudes are somewhat larger than the THEMIS data.

[34] While the THEMIS crossing cannot verify the existence of the electron vortices, the small-scale, short-duration changes observed in the magnetic fields and drifts are consistent with the properties of the vortices as seen in the simulation.

5. Summary and Discussion

[35] We have used 2D PIC simulations to investigate the process of collisionless magnetic reconnection in a config-

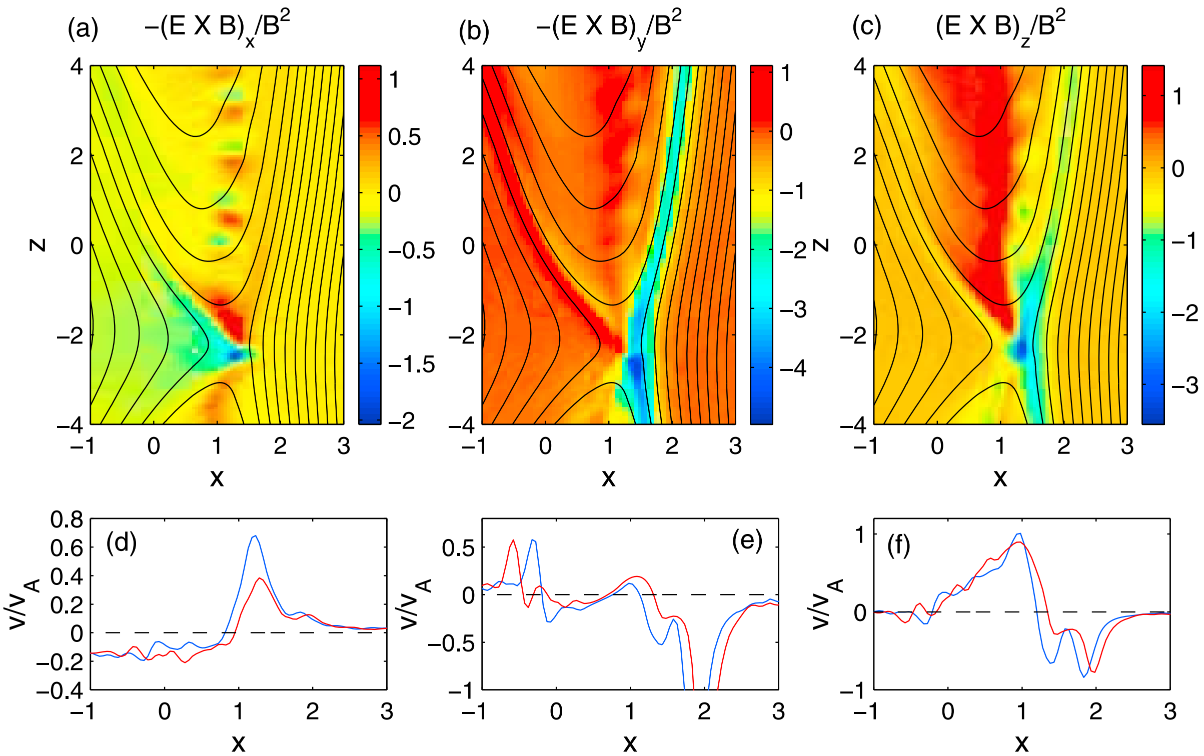

Figure 11. Simulation results at time $\Omega_{i0}t = 80$ for (a–c) the $c\mathbf{E} \times \mathbf{B}/V_AB^2$ drifts. (d–f) Profiles as a function of x for the drifts at $z = 0.6$ (blue curves) and $z = 1.6$ (red curves).

uration that models the subsolar magnetopause. The initial current sheet contained a reversing magnetic field B_z whose asymptotic magnitude increased by a factor of three from the magnetosheath to the magnetosphere, a density decrease by a factor of ten from the magnetosheath to the magnetosphere, and an initial guide magnetic field equal to the magnetosheath B_z field. The resulting ion beta value in the magnetosheath was $\beta_{i,sh} = 3.0$. The reconnection process was driven by applying a spatially localized and temporally steady convection electric field at the magnetosheath boundary.

[36] The most significant effect of the guide field was to introduce a pronounced north-south asymmetry around the X line. The in-plane Hall currents were dominated by the electron flows along the separatrices from the high-density magnetosheath side to the low-density magnetosphere side. These currents strongly enhanced the B_y field on one side of the X line (northward (southward) for a dawnward (duskward) guide field) and decreased it on the other. The electron beta along the magnetosheath separatrix was of the order of unity on the enhanced magnetic field side, while it was an order of magnitude larger on the decreased magnetic field side. On the enhanced magnetic field side were a bipolar pair of parallel electric fields and an electron velocity shear flow layer, both extending several d_i away from the X line. These structures were absent on the low magnetic field side.

[37] The Ohm's law $(\mathbf{E} + \mathbf{U}_e \times \mathbf{B}/c)_y = 0$ was found to be violated both in the immediate vicinity of the X line (electron inertial scale) and in the electron velocity shear region (ion inertial scale). For the former, the right hand side of the Ohm's law received comparable contributions from the divergence of the electron pressure tensor and the electron inertial terms, while for the latter the contributions were almost entirely from the electron pressure divergence. The region in which $(\mathbf{E} + \mathbf{U}_i \times \mathbf{B}/c)_y \neq 0$ did not encompass the electron velocity shear region, and thus the electron "diffusion" region was not contained within the ion "diffusion" region.

[38] *Scudder et al.* [2008] have argued that the key criterion characterizing the reconnection site is whether the electrons are demagnetized or not. They proposed two quantities as being useful in testing whether this condition is satisfied: the electron agyrotropy and the Lorentz ratio $\Gamma_{\perp,e}$ (equation 5). The numerator in the definition of $\Gamma_{\perp,e}$ is given by $|\mathbf{E}_\perp + \mathbf{U}_e \times \mathbf{B}/c|$, and in the present asymmetric configuration this term is large along the magnetosphere separatrix due to the large polarization electric field there. If this field is removed from the definition of $\Gamma_{\perp,e}$, then the electromagnetic $\tilde{\Gamma}_{\perp,e}$ is quite small ($\lesssim 0.1$) everywhere. The electron agyrotropy is enhanced on the magnetosphere separatrix, but it does not mark either the immediate electron scale region around the X line or the larger electron shear flow region.

[39] Even though the present simulation was driven at a steady rate, there was an inherent time dependence in the structure of the reconnection site in which a series of electron vortices was ejected from the electron velocity shear layer on the enhanced B_y side of the X line. These vortices had a size of $\sim 0.3d_i$ ($\sim 4d_e$ with the m_i/m_e ratio of 200) and propagated at a speed of about $0.3v_A$. The vortices produce large-amplitude (~30%–40%), short-duration (a few tenths of a second) modulations that reduce the magnitude of the out-of-plane field B_y. Evidence for such field

perturbations was found in a THEMIS magnetopause crossing. The vortices occur in a region where the magnetic field is not frozen-in to the electrons, and this region expands away from the X line along with the vortices as a function of time.

[40] The generation mechanism for the vortices appears to be a Kelvin-Helmholtz instability in the electron velocity shear layer. These vortices are associated with a fluctuating $\mathbf{J} \cdot \mathbf{E}$, but this contribution is small compared to the energy conversion near the X line. The mechanism for the generation of the vortices appears to be different from that in the reconnection simulation of *Drake et al.* [1997]. In that work the electron magnetohydrodynamic equations (two-fluid equations with the neglect of the ion motion) were used to study the behavior of electron current layers in 3D during collisionless reconnection. It was found that when the current width was reduced below d_e, the layer broke up into a turbulent distribution of swirling vortices as a result of a shear-flow instability. In the present case the dynamics of the simulation are only 2D, and the thickness of the electron shear layer is much larger than d_e. It has been shown in 3D PIC simulations [*Zeiler et al.*, 2002] that current layers below the d_e scale do not form during reconnection because the heating of the electrons as they flow into the low magnetic field near the X line causes the electron gyro-excursion across the X line to exceed d_e. Nevertheless, it would be interesting to determine the behavior of the present electron shear layer in 3D.

[41] The generation of the electron vortices is related to the formation of a velocity shear layer between the separatrices in which $\partial U_{ez}/\partial x$ has a sign opposite to the shears in U_{ez} at the inside edges of the separatrices. This gives a vorticity which is in the same direction as the guide field. This feature appears to be unique to the case of asymmetric reconnection with a guide field. In an asymmetric configuration without a guide field, there is no longer a preferred out-of-plane direction in the initial configuration. The strong variation of the E_x field then does not produce a localized reversal of the U_{ez} flow. In the symmetric reconnection case with a small asymptotic density, the guide field case is dominated by the formation of low density cavities on one pair of separatrices where well-defined electron beams are formed due to acceleration by the parallel electric field and directed into the X line [*Pritchett and Coroniti*, 2004]. The streaming of these beam electrons relative to the ions can lead to the production of electron holes as a consequence of the excitation of the Buneman instability [*Drake et al.*, 2003; *Cattell et al.*, 2005; *Pritchett*, 2005; *Goldman et al.*, 2008]. The electron outflow is concentrated on the opposite pair of separatrices, and no shear layer is formed in between. In the asymmetric case the large magnetosheath density prevents the formation of the low-density cavities and the high-speed beams.

[42] **Acknowledgments.** One of us (P.L.P.) would like to thank F. V. Coroniti for valuable discussions. This research was supported by NASA grants NNG08AM15G, NNG05GL27G, and NNG05GC72G and contract NAS5-02099–07/09. The particle simulations were performed using resources of the San Diego Supercomputer Center (supported by the National Science Foundation under cooperative agreement ACI-9619020), the National Energy Research Scientific Computing Center (supported by the Office of Science of the U.S. Department of Energy under contract DE-AC03-76SF00098), and the UCLA Dawson Cluster (funded by NSF grant PHY-0321345).

[43] Amitava Bhattacharjee thanks the reviewers for their assistance in evaluating this paper.

References

Birn, J., and E. R. Priest (Eds.) (2007), *Reconnection of Magnetic Fields*, chap. 3, p. 87, Cambridge Univ. Press, Cambridge, U. K.
Cassak, P. A., and M. A. Shay (2007), Scaling of asymmetric magnetic reconnection: General theory and collisional simulations, *Phys. Fluids*, *14*, 102114, doi:10.1063/1.2795630.
Cattell, C., et al. (2005), Cluster observations of electron holes in association with magnetotail reconnection and comparison to simulations, *J. Geophys. Res.*, *110*, A01211, doi:10.1029/2004JA010519.
Ding, D. Q., L. C. Lee, and D. W. Swift (1992), Particle simulations of driven collisionless magnetic reconnection at the dayside magnetopause, *J. Geophys. Res.*, *97*, 8453.
Drake, J. F., D. Biskamp, and A. Zeiler (1997), Breakup of the electron current layer during 3-D collisionless magnetic reconnection, *Geophys. Res. Lett.*, *24*, 2921.
Drake, J. F., M. Swisdak, C. Cattell, M. A. Shay, B. N. Rogers, and A. Zeiler (2003), Formation of electron holes and particle energization during magnetic reconnection, *Science*, *299*, 873.
Drake, J. F., M. Swisdak, K. M. Schoeffler, B. N. Rogers, and S. Kobayashi (2006), Formation of secondary islands during magnetic reconnection, *Geophys. Res. Lett.*, *33*, L13105, doi:10.1029/2006GL025957.
Goldman, M. V., D. L. Newman, and P. L. Pritchett (2008), Vlasov simulations of electron holes driven by particle distributions from PIC simulations with a guide field, *Geophys. Res. Lett.*, *35*, L22109, doi:10.1029/2008GL035608.
Harris, E. G. (1962), On a plasma sheath separating regions of oppositely directed magnetic field, *Nuovo Cimento*, *23*, 115.
Hesse, M., M. Kuznetsova, and J. Birn (2004), The role of electron heat flux in guide-field magnetic reconnection, *Phys. Plasmas*, *11*, 5387.
Huang, J., Z. W. Ma, and D. Li (2008), Debye-length scaled structure of perpendicular electric field in collisionless magnetic reconnection, *Geophys. Res. Lett.*, *35*, L10105, doi:10.1029/2008GL033751.
Karimabadi, H., W. Daughton, and K. B. Quest (2005a), Physics of saturation of collisionless tearing mode as a function of guide field, *J. Geophys. Res.*, *110*, A03214, doi:10.1029/2004JA010749.
Karimabadi, H., W. Daughton, and K. B. Quest (2005b), Antiparallel versus component merging at the magnetopause: Current bifurcation and intermittent reconnection, *J. Geophys. Res.*, *110*, A03213, doi:10.1029/2004JA010750.
Karimabadi, H., W. Daughton, and J. Scudder (2007), Multi-scale structure of the electron diffusion region, *Geophys. Res. Lett.*, *34*, L13104, doi:10.1029/2007GL030306.
Miura, A., and P. L. Pritchett (1982), Nonlocal stability analysis of the MHD Kelvin-Helmholtz instability in a compressible plasma, *J. Geophys. Res.*, *87*, 7431.
Mozer, F. S., and P. L. Pritchett (2009), Regions associated with electron physics in asymmetric magnetic field reconnection, *Geophys. Res. Lett.*, *36*, L07102, doi:10.1029/2009GL037463.
Mozer, F. S., and A. Retinò (2007), Quantitative estimates of magnetic field reconnection properties from electric and magnetic field measurements, *J. Geophys. Res.*, *112*, A10206, doi:10.1029/2007JA012406.
Mozer, F. S., P. L. Pritchett, J. Bonnell, D. Sundkvist, and M. T. Chang (2008), Observations and simulations of asymmetric magnetic field reconnection, *J. Geophys. Res.*, *113*, A00C03, doi:10.1029/2008JA013535.
Phan, T. D., J. F. Drake, M. A. Shay, F. S. Mozer, and J. P. Eastwood (2007), Evidence for an elongated (>60 ion skin depths) electron diffusion region during fast magnetic reconnection, *Phys. Rev. Lett.*, *99*, 255002, doi:10.1103/PhysRevLett.99.255002.
Pritchett, P. L. (2001), Geospace Environment Modeling magnetic reconnection challenge: Simulations with a full particle electromagnetic code, *J. Geophys. Res.*, *106*, 3783.
Pritchett, P. L. (2005), Onset and saturation of guide-field magnetic reconnection, *Phys. Plasmas*, *12*, 062301, doi:10.1063/1.1914309.
Pritchett, P. L. (2008), Collisionless magnetic reconnection in an asymmetric current sheet, *J. Geophys. Res.*, *113*, A06210, doi:10.1029/2007JA012930.
Pritchett, P. L., and F. V. Coroniti (1998), Interchange instabilities and localized high-speed flows in the convectively-driven near-Earth plasma sheet, in *Substorms-4*, edited by S. Kokubun and Y. Kamide, p. 443, Kluwer Acad., Norwell, Mass.
Pritchett, P. L., and F. V. Coroniti (2004), Three-dimensional collisionless magnetic reconnection in the presence of a guide field, *J. Geophys. Res.*, *109*, A01220, doi:10.1029/2003JA009999.
Ricci, P., J. U. Brackbill, W. Daughton, and G. Lapenta (2004), Collisionless magnetic reconnection in the presence of a guide field, *Phys. Plasmas*, *11*, 4102.
Roux, A., O. Le Contel, C. Coillot, A. Bouabdellah, B. de la Porte, D. Alison, S. Ruocco, and M. C. Vassal (2008), The search coil magnetometer for THEMIS, *Space Sci. Rev.*, *141*, 265, doi:10.1007/s11214-008-9455-8.

Scholer, M., I. Sidorenko, C. H. Jaroschek, R. A. Treumann, and A. Zeiler (2003), Onset of collisionless magnetic reconnection in thin current sheets: Three-dimensional particle simulations, *Phys. Plasmas*, *10*, 3521.

Scudder, J., and W. Daughton (2008), ''Illuminating'' electron diffusion regions of collisionless magnetic reconnection using electron agyrotropy, *J. Geophys. Res.*, *113*, A06222, doi:10.1029/2008JA013035.

Scudder, J. D., R. D. Holdaway, R. Glassberg, and S. L. Rodriguez (2008), Electron diffusion region and thermal demagnetization, *J. Geophys. Res.*, *113*, A10208, doi:10.1029/2008JA013361.

Shay, M. A., J. F. Drake, and M. Swisdak (2007), Two-scale structure of the electron dissipation region during collisionless magnetic reconnection, *Phys. Rev. Lett.*, *99*, 155002, doi:10.1103/PhysRevLett.99.155002.

Sonnerup, B. U. Ö., I. Papamastorakis, G. Paschmann, and H. Lühr (1987), Magnetopause properties from AMPTE/IRM observations of the convection electric field: Method development, *J. Geophys. Res.*, *92*, 12,137.

Swisdak, M., B. N. Rogers, J. F. Drake, and M. A. Shay (2003), Diamagnetic suppression of component magnetic reconnection at the magnetopause, *J. Geophys. Res.*, *108*(A5), 1218, doi:10.1029/2002JA009726.

Tanaka, K. G., et al. (2008), Effects on magnetic reconnection of a density asymmetry across the current sheet, *Ann. Geophys.*, *26*, 2471.

Walén, C. (1944), On the theory of sunspots, *Ark. Mat. Astron. Fys.*, *30A*(15), 1.

Zeiler, A., D. Biskamp, J. F. Drake, B. N. Rogers, M. A. Shay, and M. Scholer (2002), Three-dimensional particle simulations of collisionless reconnection, *J. Geophys. Res.*, *107*(A9), 1230, doi:10.1029/2001JA000287.

F. S. Mozer, Space Sciences Laboratory, University of California, Berkeley, CA 94720, USA. (fmozer@ssl.berkeley.edu)

P. L. Pritchett, Department of Physics and Astronomy, University of California, 405 Hilgard Ave., Los Angeles, CA 90095-1547, USA. (pritchet@physics.ucla.edu)